



OPEN

Correlation versus hybridization gap in CaMn_2Bi_2

Christopher Lane^{1,2}✉, M. M. Piva^{3,4}, P. F. S. Rosa⁵ & Jian-Xin Zhu^{1,2}✉

We study the interplay between electronic correlations and hybridization in the low-energy electronic structure of CaMn_2Bi_2 , a candidate hybridization-gap semiconductor. By employing a DFT+ U approach we find both the antiferromagnetic Néel order and band gap in good agreement with the corresponding experimental values. Under hydrostatic pressure, we find a crossover from hybridization gap to charge-transfer insulating physics due to the delicate balance of hybridization and correlations. Increasing the pressure above $P_c = 4$ GPa we find a simultaneous pressure-induced volume collapse, plane-to-chain, insulator to metal transition. Finally, we have also analyzed the topology in the antiferromagnetic CaMn_2Bi_2 for all pressures studied.

The electronic structure of fermionic correlated systems is driven by the competition between the tendencies of the electron to spread out as a wave and to localize as a particle, the latter usually accompanied with magnetism. That is, the interplay of the spin and charge degrees of freedom is a central issue¹. Layered two-dimensional (2D) materials provide a unique platform for studying this dual nature of the electronic states which produces rich phase diagrams including high temperature superconductivity^{2–4}, non-trivial topological insulating and semi-metallic phases⁵, quantum spin liquid states⁶, and strange metal behavior⁷.

In particular, the iron-based superconductors have been under vigorous experimental and theoretical study since the discovery of unconventional high-temperature superconductivity in $\text{La}[\text{O}_{1-x}\text{F}_x]\text{FeAs}$ in 2008⁸. Since then a family of compounds with related layered crystal structures and chemical compositions were discovered including FeSe , LiFeAs , $R\text{FeAsO}$ (R = rare earth), $A\text{Fe}_2\text{As}_2$ (A = Ca, Sr, Ba, Eu), termed the ‘11’, ‘111’, ‘1111’, and ‘122’ type structures, respectively⁹. The highest superconducting transition temperature of 56 K has been found in the 1111-type compound $\text{Gd}_{0.8}\text{Th}_{0.2}\text{FeAsO}$ ¹⁰.

To enhance the superconducting transition temperature and search for new broken symmetry phases, Fe was substituted away and replaced by other transition metals such as Cr, Mn, Co, and Ni. These isostructural compounds form new ground states including metallic (Co-based), itinerant antiferromagnetic (Cr-based), superconducting (Ni-based), and semiconducting antiferromagnetic (Mn-based) behavior. The Mn-based pnictides garnered special interest due to their similarity to the phenomenology of the high-temperature cuprate superconductors. In particular, the Mn-based compounds exhibit insulator-metal transitions upon either doping or application of pressure, but superconductivity has yet to be reported^{11–17}, even though pressure induced superconductivity is observed in other Mn-based materials^{18,19}. In general this suggests that the manganese pnictides possibly form a bridge between the pnictide and cuprate material families.

Recent experimental and theoretical studies find CaMn_2Bi_2 to host many intriguing properties including large anisotropic magnetoresistance²⁰ and a plane-to-chain structural transition²¹. Most intriguingly, it has been suggested that CaMn_2Bi_2 may be a hybridization-gap semiconductor^{22,23}. In line with this claim, low-temperature electrical transport measurements find a slight increase of the gap under pressure²⁴. This type of behavior is akin to $\text{Ce}_3\text{Bi}_4\text{Pt}_3$ and other heavy fermion compounds^{25–27}. Therefore, CaMn_2Bi_2 could provide a link between the cuprates, pnictides, and heavy fermion systems.

In this article, we present a first-principles investigation of the electronic and magnetic structure of CaMn_2Bi_2 . We find the delicate balance between electronic correlations and hybridization to depend sensitively on pressure, resulting in a non-monotonic behavior of the band gap. In the pristine case, we are able to obtain an accurate ground state by including an effective Hubbard U , which significantly improves the agreement with experiments over earlier theoretical studies where GGA-PBE predicts a metal²², while hybrid functional dramatically overestimates the gap by an order-of-magnitude²⁴. The good agreement also provides an important starting point for the study of pressure effects. Under applied hydrostatic pressure, we find CaMn_2Bi_2 to behave as a

¹Theoretical Division, Los Alamos National Laboratory, Los Alamos, NM 87545, USA. ²Center for Integrated Nanotechnologies, Los Alamos National Laboratory, Los Alamos, NM 87545, USA. ³Max Planck Institute for Chemical Physics of Solids, Nöthnitzer Str. 40, 01187 Dresden, Germany. ⁴Instituto de Física “Gleb Wataghin”, UNICAMP, Campinas, SP 13083-859, Brazil. ⁵Division of Materials Physics and Application, Los Alamos National Laboratory, Los Alamos, NM 87545, USA. ✉email: laneca@lanl.gov; jxzhu@lanl.gov

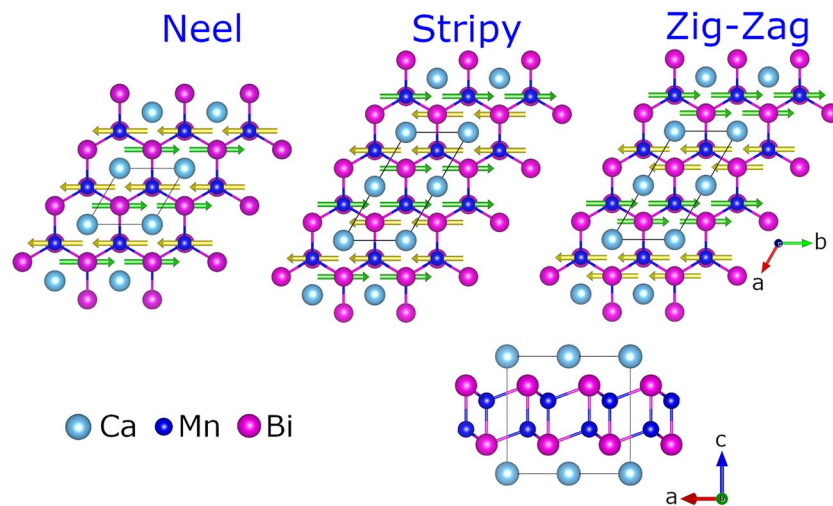


Figure 1. Various antiferromagnetic ground state configurations within the crystal structure of CaMn_2Bi_2 . Green (gold) arrows represent the positive (negative) manganese magnetic moments. The stacking of the atomic layers is shown on the lower right. The black lines mark the unit cell.

hybridization gap material up to 3 GPa and a correlation driven compound for larger pressures. Most strikingly, we find a large volume collapse due to a plane-to-chain structural transition at $P_c = 4$ GPa, which simultaneously produces a metallic ground state. Moreover, the spin (orbital) manganese magnetic moments significantly decrease (increase) across the critical pressure. The predicted critical pressure and volume collapse are in good accord with experimental values²¹. Finally, we also find the antiferromagnetic CaMn_2Bi_2 to be topologically trivial for all studied pressures.

Results

Magnetic and electronic structure. Figure 1 shows the three possible antiferromagnetic ground state configurations within the crystal structure of CaMn_2Bi_2 . The magnetic moments (green and gold arrows) are stabilized on the manganese sites within the plane oriented along the b -axis in accord with experimental observations²². Our first principles total energy calculations find the Néel-type order to be the ground state consistent with neutron diffraction²², with the other candidate magnetic states lying at least 35 meV/Mn above in energy. The magnitude of the magnetic moments along with the band gap and relative total energy of the various magnetic configurations are given in Table 1. Experimentally, the Néel phase exhibits a magnetic moment of $3.85 \mu_B$ and a band gap between 31 and 62 meV, depending on the report^{22,28}. Additional recent transport studies find a small activation gap between 2 and 4 meV²⁴. Our PBE-based calculations yield a magnetic moment close to the experimental value, but with a zero energy gap. We have also tested the new state-of-the-art density meta-GGA functional SCAN and find a slightly enhanced magnetic moments with a concomitant ~ 200 meV band gap. Curiously, this enhancement in band gap and magnetic moments is not found in studies of the cuprates^{29–33}, iridates³⁴, and 3d perovskite oxides in general³⁵.

To remedy the underestimation of the band gap, we introduce an effective U on the Mn- d states within the GGA+ U scheme of Dudarev et al.³⁶ To find the U that yields the experimental values, a range of on-site Hubbard interaction values were considered. Figure 2 (right panel) shows the evolution of the band gap, the total (dash-dot lines), spin, and orbital (solid lines) magnetic moments as a function of U for the various magnetic configurations, along with the average experimental values overlaid (violet shading). Increasing U from 0.0 to 2.0 eV a band gap opens in the Néel and Zig-Zag phases, while the gap in the Stripy arrangement increases monotonically. For U greater than 3.0 eV, the gap in the Stripy and Néel orders decrease, while that of the Zig-Zag phase flattens. This non-monotonic behavior is observed in a number of oxide materials including MnO_2 ³⁷, TiO_2 ³⁸ and possibly in the superconducting infinite-layer nickelates³⁹, though self-doping effects may be at play in this compound. Simultaneously, the strength of the spin (orbital) magnetic moments continually increase (decrease) with increasing U . Since the finite orbital moment is induced on the manganese atom via hybridization with the p -orbitals on the bismuth atoms with strong spin-orbit coupling, the decrease in this moment with U shows clearly a correlation-induced reduction of hybridization between the atomic species, in favor of electron localization on the Mn site. This localization process concomitantly drives the increase in the size of the spin component of the moment. A U of 4.75 eV is found to reproduce the experimentally measured gap value while only enhancing the magnetic moment by $\sim 0.5 \mu_B$, as indicated by the black dotted line. Furthermore, our calculations find the b -axis magnetic orientation, as determined by the experiment, to be most stable by 0.1 meV compared to the axis perpendicular to b . To cross check our U_{eff} , we calculated the Hubbard U derived from the screened F^0 Slater integral following the procedure given by Madsen and Novák⁴⁰ as implemented in Wien2k⁴¹. Within this approach, we find an effective U of 4.38 eV on Mn $3d$ electrons, in agreement with our VASP obtained value. Finally, we note these GGA+ U results improve upon those obtained using the HSE06 hybrid functional²⁴.

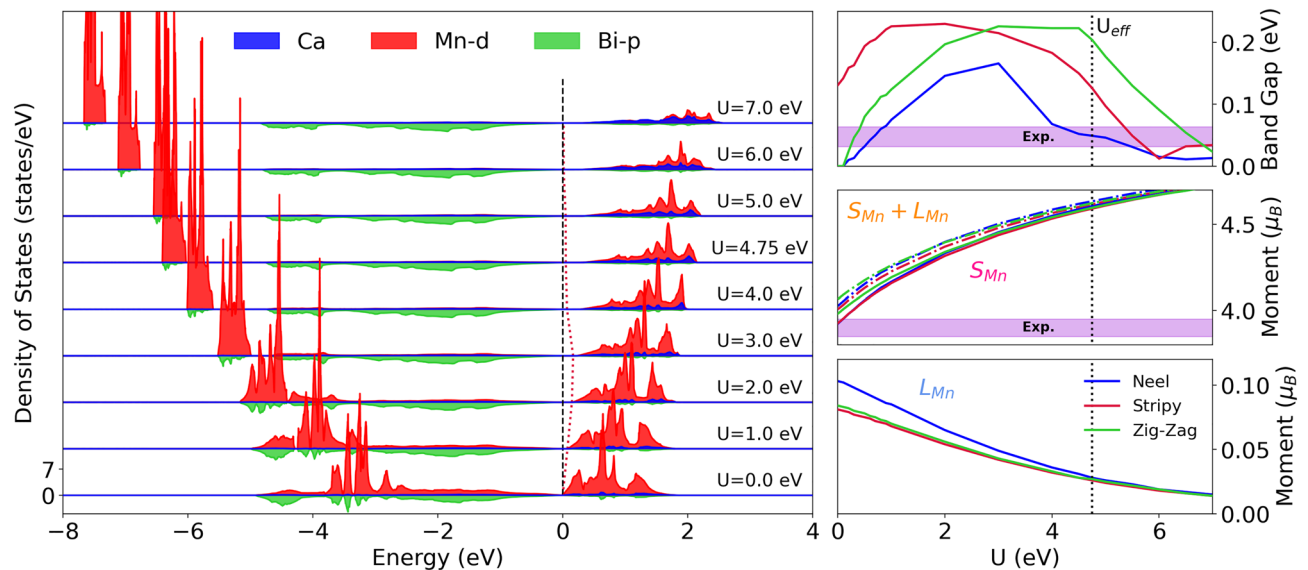


Figure 2. (left panel) Site-resolved partial density of states for the Néel AFM phase for various values of U . Shading and lines of various colors (see legend) give the contributions from manganese- d and bismuth- p orbitals, and Ca atomic weight. The red dashed line marks the leading conduction band edge, with the black dashed line marking the Fermi Energy. For a zoom-in of the band gap see Fig. S4 in the Supplemental Information. (right panel) The spin and orbital (solid lines) components of the total (dot-dashed lines) magnetic moment, along with the band gap as a function of the on-site potential U .

Order	Magnetic (μ_B)	Orbital (μ_B)	Total (μ_B)	Gap (meV)	Relative energy (meV/Mn)
DFT					
Néel	3.923	0.103	4.026	0	0
Stripy	3.926	0.081	4.007	131	35
Zig-Zag	3.981	0.084	4.065	0	108
DFT+U					
Néel	4.606	0.028	4.634	49	0
Stripy	4.591	0.026	4.617	126	22
Zig-Zag	4.596	0.027	4.623	204	42

Table 1. Comparison of various theoretically predicted properties for the three possible antiferromagnetic ground states in CaMn_2Bi_2 using DFT and DFT+ U ($U = 4.75$ eV).

Figure 2 (left panel) shows the site-resolved density of states (DOS) for various atomic orbitals including Mn- d , Bi- p , and total Ca weight as a function of the effective U . On tuning U from 0 to 1 eV the gap in the magnetically split Mn- d states (centered at -3 eV and 1.0 eV) clearly expands, marking a rise in the Mn- d on-site correlations. Importantly, a finite gap opens at the Fermi level, with Mn- d dominating the valence and conduction bands. As U is increased from 1 to 3 eV, manganese character decreases from the band edges due to the increased on-site correlations. At a Hubbard U value of 3 eV, the electronic band gap transitions from Mott-like to a hybridization gap since the low energy state band edge surrounding the Fermi level are composed exclusively of bismuth p -orbital character. For $U > 3$ eV the manganese levels continue to move to higher (lower) energies in conduction (valence) band exposing more bismuth density of states. See the Supplemental Information for a detailed close up of the Fermi level. For U equal to 4.75 eV, the Mn- d states sit slightly above (~ 4 meV) the Bi- p levels in the conduction band. We note spin-orbit coupling plays a significant role in reducing the overall electronic band gap, see the Supplemental Information for details. The evolution of the electronic states with on-site correlations clearly demonstrates the critical role the Hubbard U parameter plays in achieving the correct delicate balance between correlation and hybridization in this compound.

Figure 3 shows the electronic band structure of CaMn_2Bi_2 in the Néel AFM phase with (blue) and without (red) the effective Hubbard U of 4.75 eV. Interestingly, the effective on-site correlations appear to change the relative energy of the conical band at Γ and the narrow band at M in the conduction bands. Specifically, for U equal to 4.75 eV, an indirect to direct transition is precipitated, the band extrema of the conduction and valence bands change from Γ and M , respectively, to centered at Γ . In the valence states, the band structure resembles that obtained purely by the generalized gradient approximation^{22,24}. In contrast, the conduction bands obtained

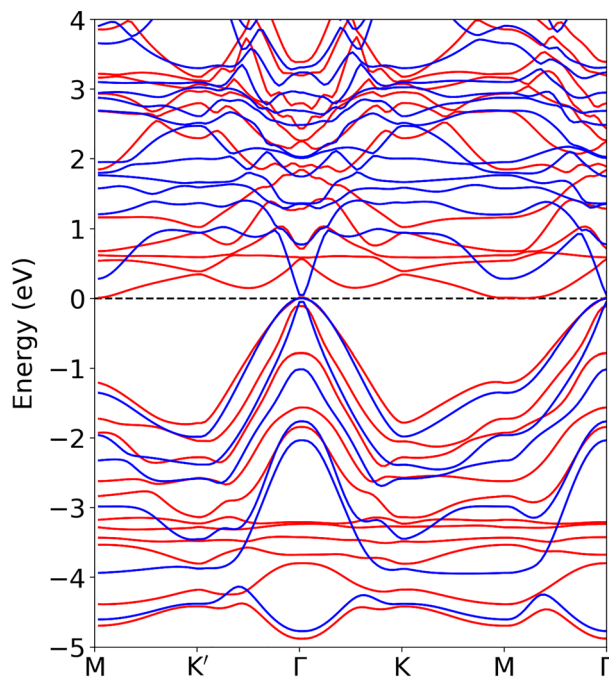


Figure 3. Electronic band dispersion of CaMn_2Bi_2 in the Néel AFM phase with (blue lines) and without (red lines) an effective on-site potential U of 4.75 eV.

by the HSE06 hybrid functional (Ref.²⁴) are more dispersive and display characteristically different transitions, which should be noticeable in optical spectroscopy.

We further note that upon introducing a U of 4.75 eV the relative energy between the different AFM ground state configurations has changed. Now we find the Néel and Stripy types to be separated by 22 meV/Mn, while the energy difference to the Zig-Zag ordered state is 42 meV/Mn, making the Stripy and Zig-Zag phases irrelevant in the ground state. For more details see the Supplemental Information.

Effect of pressure. Applied external pressure provides a direct means to assess the relative ratio between hybridization and correlation strengths in a material. If the band gap is driven by correlations, pressure squeezes the lattice sites of the crystal closer together forcing the wave functions of neighboring atomic sites to overlap. Electrons then tend to become more delocalized in the material, yielding a metal. In contrast, if the band gap is governed by hybridization, pressure further separates bonding and anti-bonding states, thus increasing the band gap. When both hybridization and correlations are present, the gap can undergo non-monotonic behavior under pressure as a result of their competition.

Figure 4e,f shows the site-resolved partial density of states in the Néel-type antiferromagnetic phase of CaMn_2Bi_2 under hydrostatic pressures from 0 to 8 GPa. At zero pressure the AFM order opens a gap of 49 meV, consistent with the range of reported experimental values. As pressure is applied, the energy separation between the bismuth states surrounding the band gap increases, due to the enhanced hybridization. In contrast, the separation between manganese states above and below the Fermi level decreases. There is also a concomitant slight broadening of the states possibly marking an enhancement of Mn- d and Bi- p hybridization. In addition, we have calculated the orbital-dependent hybridization function by treating Mn- $3d$ as correlated orbitals within the dynamical mean-field theory and find a two-fold increase in the hybridization function, which further corroborates this enhancement in hybridization in the low pressure regime. Furthermore, we have also performed a non-spin-polarized DFT+ U calculations to examine the effect of pressure in lieu of spin splitting and also find a marked increase in the direct band gap, indicative of an enhancement of the hybridization with pressure, see the Supplemental Information for details. As the hydrostatic pressure is increased to 3 GPa the Mn- d and Bi- p levels cross. This changes the character of the conduction band edge from exclusively bismuth to manganese, thereby transforming the compound from a hybridization gap material to a charge-transfer insulator. The pressure of 3 GPa also marks a reversal from positive to negative of the band gap derivative with pressure. The red dashed line follows the evolution of the leading edge of the conduction band and clearly traces out a non-monotonic path with pressure (Fig. 4).

The low pressure behavior of the gap can be rationalized as follows. For small hydrostatic pressures the band gap increases due to the increases in wave function overlap between neighboring atomic lattice sites. However, once pressure becomes too large, the magnetic correlations begin to collapse eventually pulling Mn- $3d$ states towards the Fermi level, all while the bismuth levels shift further away from the Fermi energy. Therefore, the hybridization plays a dual role by separating bismuth states at the bands edges, while simultaneously killing magnetic correlations; annihilating the gap. This suggests that CaMn_2Bi_2 is on the boundary between a correlated

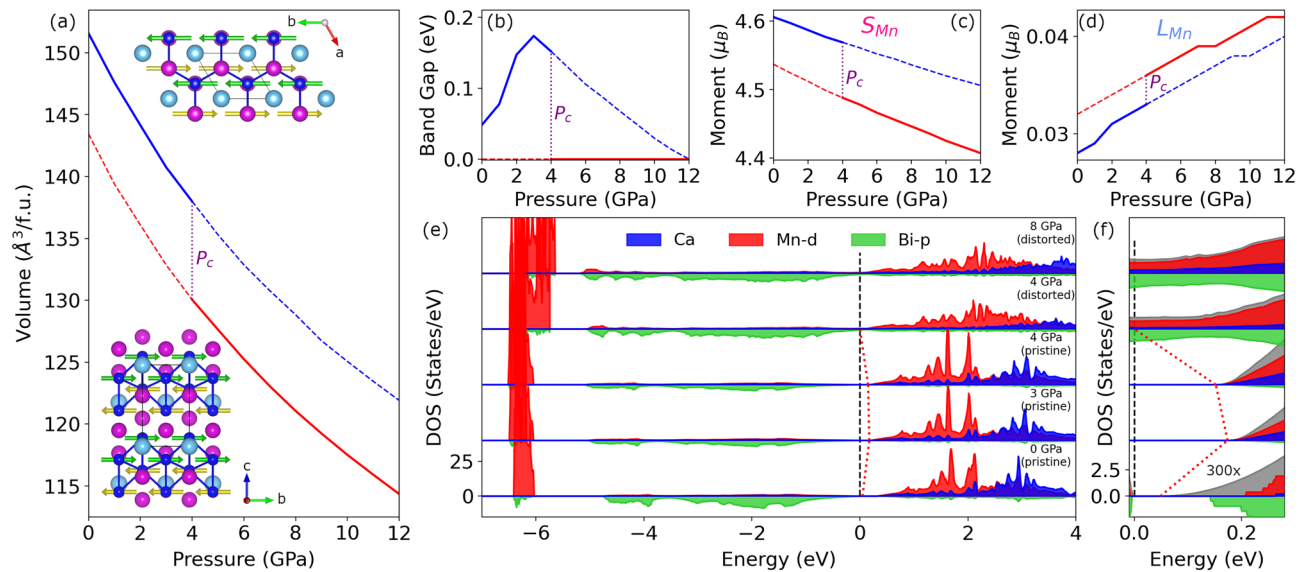


Figure 4. (a) Volume per formula unit of CaMn_2Bi_2 in the Néel type antiferromagnetic phase for both the pristine (blue) and distorted (red) crystal structures using DFT+ U ($U=4.75$ eV) for various values of pressure. The color of the various atomic species in the crystal structures are the same as in Fig. 1. (b) The band gap, along with the (c) spin and (d) orbital components of the total magnetic moment in the pristine (blue) and distorted (red) crystal structures as a function of pressure. The solid (dashed) lines indicate that the given crystalline phase is stable (unstable). (e) Site-resolved partial density of states in the Néel type antiferromagnetic phase of CaMn_2Bi_2 under various values of pressure. Shading and lines of various colors (see legend) give the contributions from manganese- d and bismuth- p orbitals, and total Ca atomic weight. Red solid line tracks the leading edge of the conduction states as the system passes through an insulator-metal transition. Black dashed line marks the Fermi Energy. (f) Zoom-in of the band gap in the partial density of states in (e) with the zero pressure density of states enhanced by 300x to make the tail of the band edge visible. The grey shading and lines indicate the total density of states.

charge-transfer insulator and a hybridization gap semiconductor, thereby providing a possible link between the cuprates, pnictides, and heavy fermion systems.

If the pressure is further increased beyond 4 GPa, the planar honeycomb lattice of manganese atoms becomes unstable. To lower the global total energy of the system, a Mn atom slides along the a -axis forming a quasi-one-dimensional chain structure. By tracking the enthalpy versus pressure of the two crystalline phases (see the Supplemental Information), we find the structural transition to occur at a critical pressure P_c of 4 GPa in accord with experiment²¹. At this pressure, we predict a dramatic effect on many of the key properties of CaMn_2Bi_2 .

Figure 4a–d shows various key properties of the pristine (blue) and distorted (red) crystal structures for the various pressures, where the relative stability of the two structures is indicated by the solid (stable) and dashed (unstable) lines. At P_c , our calculations yield a $8 \text{ \AA}^3/\text{f.u.}$ volume collapse across the boundary, while simultaneously, there is an appreciable jump down (up) in the spin (orbital) magnetic moment. Beyond P_c the spin (orbital) magnetic moment steady decreases (increases), again illustrating the competition between hybridization and correlations. The spin magnetization provides a direct indicator of the strength of correlations, while the orbital component tracks the overlap of Bi and Mn atomic wave functions. Furthermore, hybridization between bismuth and manganese atomic wave functions induces an effective spin-orbit coupling on the Mn sites. Finally, this pressure induced plane-to-chain transition also gives way to an insulator to metal transition at P_c . We note that theoretical calculations using isotropic expansion and compression were unable to find any energy-equivalent point between the two crystal phases²¹. Here, the mixture of GGA+ U and relaxing both the atomic positions and unit cell shape are able to capture the essential physics and lattice degrees of freedom to yield observable results.

Such pressure induced volume collapses can be classified into three categories of mechanisms: correlation driven (e.g. heavy fermion compounds⁴²), Jahn-Teller effect (e.g. KCuF_3 ⁴³), and Peierls-distortion (e.g. NbSe_3 ⁴⁴). Here, since there is no Fermi surface in the pristine phase no nesting between the various Fermi sheets can occur, ruling out a Peierls-distortion as a possible mechanism. Typically, Jahn-Teller driven effects stem from a change in the d electron count. For example, the coordination of the transition metals in the transition metal dichalcogenides varies systematically with d electron count between trigonal-prismatic, octahedral, and distorted octahedra (forming quasi-one-dimensional chains)⁴⁵, with the latter distorted structure being characterized as Jahn-Teller driven⁴⁶. For the present material under examination, we only find a marginal increase in the total charge of the Wigner-Seitz sphere, making the Jahn-Teller process unlikely. Therefore, our results suggest that the pressure-induced volume collapse (plane-to-chain) insulator to metal transition is mainly driven by correlation effects.

Topological character. Originally, CaMn_2Bi_2 was thought to be a possible magnetic 3D Dirac semimetal, where the Mn-*d* states were assumed to behave as core electrons⁴⁷. This then allows for a clean band inversion of Bi-*s* and Bi-*p* levels. However, Gibson et al.²² found that the Mn-*d* orbitals play a significant role at the Fermi level, hybridized with the manifold of bismuth states. This ultimately disrupts the Bi-*s* and Bi-*p* level, avoiding a topological non-trivial ground state.

To confirm the topological nature of CaMn_2Bi_2 we used the vasp2trace code⁴⁸ in conjunction with the Check Topological Material module^{49–51} provided on the Bilbao Crystallographic Server.^{52–54} CaMn_2Bi_2 is indeed found to be topological trivial for all pressures up to 12 GPa, due to the fact that the Mn-*d* levels dominate the low energy electronic structure and prevent the Bi-*s* and *p* states to overlap and invert. However, if the on-site energy of the manganese bands were to be tuned away from the Fermi level or the Bi-*s* state brought closer to the Fermi level, the bismuth *s* and *p* level could be inverted, making the ground state topologically non-trivial.

Discussion

In the original analysis performed by Gibson et al.²² it was claimed that CaMn_2Bi_2 behaves as a hybridization gap material. This was justified by tracking only the changes in position of the Bi-*p* and *s* levels with expanding and contracting the unit cell volume by 1% without relaxation, and ignoring the Mn states which cross the Fermi level. Furthermore, after cross checking our results within VASP and Wien2k⁴¹ we find the electronic structure presented by Gibson et al. to be inconsistent. We believe the bands presented in Ref.²² are a result of an incomplete calculation workflow, where the spin-orbit coupling subroutines were possibly neglected. See the Supplemental Information for more details. Additionally, the pressure study by some of us²⁴ reports an increase in activation energy of only 20–40 K (2–4 meV) with pressure using electrical transport measurements. The gap observed in Ref.²⁴ is one order of magnitude smaller than our prediction, implying the possible existence of impurity states within the gap. The presence of impurities would make the sample sensitive to changes in external pressure and could produce anomalous transport results. Therefore, to accurately compare our first-principles results with the experimental measurements a rigorous modeling of the transport process is required. Additionally, Ref.²⁴ reported an increase in T_N with pressure. However, since our density functional theory results only produce the magnetic moment at zero temperature without any measure of the fluctuations, we cannot give any direct insight into the change in T_N with pressure.

Conclusion

From our analysis of the ground state electronic structure of CaMn_2Bi_2 as a function of pressure, we find that the low energy electronic structure manifests both correlated charge-transfer insulator and hybridization gap semiconductor characteristics. To fully elucidate its connection to the cuprates, pnictides, and heavy fermion compounds and to what extent they are similar, i.e. exhibiting charge/spin density waves and unconventional superconductivity, further doping dependent studies are needed to uncover its full phase diagram. Moreover, the addition of holes should produce an interesting interplay between itinerant antiferromagnetic carriers and those on the strongly spin-orbit coupled Bi-*p* orbitals, creating a favorable environment for new exotic phases of matter.

Methods

Ab initio calculations were carried out by using the pseudopotential projector-augmented wave method⁵⁵ implemented in the Vienna *ab initio* simulation package (VASP)^{56,57} with an energy cutoff of 600 eV for the plane-wave basis set. Exchange-correlation effects were treated using the Perdew–Burke–Ernzerhof (PBE) GGA density functional⁵⁸, where a $12 \times 12 \times 8$ Γ -centered *k*-point mesh was used to sample the Brillouin zone. Spin-orbit coupling effects were included self-consistently at all stages of the calculations. We used the low-temperature zero (high) pressure $P3m1$ ($P12_1/m1$) crystal structure in accord with the experimental measurements to initialize our calculations^{21,59}. The pressure dependence of the various physical properties of CaMn_2Bi_2 was obtained by increasing (decreasing) the hydrostatic pressure on the zero (high) pressure crystal structure in small quasi-adiabatic steps. For each *U* and pressure, all atomic sites in the unit cell along with the unit cell dimensions were relaxed simultaneously using a conjugate gradient algorithm to minimize energy with an atomic force tolerance of 0.01 eV/Å and a total energy tolerance of 10^{-6} eV. The theoretically obtained structural parameters for CaMn_2Bi_2 in the Néel state at zero pressure, $a = b = 4.76$ Å, and $c = 7.72$ Å, are in good agreement with the corresponding experimental results.

Data availability

All data supporting the findings of this study are available from the corresponding authors upon request.

Received: 31 March 2022; Accepted: 24 May 2023

Published online: 07 June 2023

References

1. Nagaosa, N. *Quantum Field Theory in Strongly Correlated Electronic Systems* (Springer, 1999).
2. Sun, L. *et al.* Re-emerging superconductivity at 48 Kelvin in iron chalcogenides. *Nature* **483**, 67 (2012).
3. Stewart, G. Superconductivity in iron compounds. *Rev. Mod. Phys.* **83**, 1589 (2011).
4. Proust, C. & Taillefer, L. The remarkable underlying ground states of cuprate superconductors. *Annu. Rev. Condens. Matter Phys.* **10**, 409 (2019).
5. Bansil, A., Lin, H. & Das, T. Colloquium: Topological band theory. *Rev. Mod. Phys.* **88**, 021004 (2016).
6. Takagi, H., Takayama, T., Jackeli, G., Khaliullin, G. & Nagler, S. E. Concept and realization of kitaev quantum spin liquids. *Nat. Rev. Phys.* **1**, 264 (2019).
7. Shen, B. *et al.* Strange-metal behaviour in a pure ferromagnetic kondo lattice. *Nature* **579**, 51 (2020).

8. Kamihara, Y., Watanabe, T., Hirano, M. & Hosono, H. Iron-based layered superconductor La $[O_{1-x}F_x]$ FeAs ($x = 0.05-0.12$) with $T_c = 26$ K. *JACS* **130**, 3296 (2008).
9. Wen, H.-H. & Li, S. Materials and novel superconductivity in iron pnictide superconductors. *Annu. Rev. Condens. Matter Phys.* **2**, 121 (2011).
10. Wang, C. *et al.* Thorium-doping-induced superconductivity up to 56 K in $Gd_{1-x}Th_xFeAsO$. *EPL* **83**, 67006 (2008).
11. Yanagi, H. *et al.* Antiferromagnetic bipolar semiconductor LaMnPO with ZrCuSiAs-type structure. *J. Appl. Phys.* **105**, 093916 (2009).
12. McGuire, M. A. & Garlea, V. O. Short- and long-range magnetic order in LaMnAsO. *Phys. Rev. B* **93**, 054404 (2016).
13. Zhang, Q. *et al.* Structure and magnetic properties of Ln MnSbO (Ln = La and Ce). *Phys. Rev. B* **93**, 094413 (2016).
14. Simonson, J. *et al.* From antiferromagnetic insulator to correlated metal in pressurized and doped LaMnPO. *Proc. Natl. Acad. Sci.* **109**, E1815 (2012).
15. Simonson, J. *et al.* Gap states in insulating LaMnPO $_{1-x}F_x$ ($x = 0-0.3$). *Phys. Rev. B* **84**, 165129 (2011).
16. Sun, Y.-L. *et al.* Insulator-to-metal transition and large thermoelectric effect in La $_{1-x}Sr_x$ MnAsO. *EPL* **98**, 17009 (2012).
17. Hanna, T. *et al.* From antiferromagnetic insulator to ferromagnetic metal: Effects of hydrogen substitution in LaMnAsO. *Phys. Rev. B* **87**, 020401 (2013).
18. Cheng, J.-G. *et al.* Pressure induced superconductivity on the border of magnetic order in MnP. *Phys. Rev. Lett.* **114**, 117001 (2015).
19. Chong, X., Jiang, Y., Zhou, R. & Feng, J. Pressure dependence of electronic structure and superconductivity of the Mn $_x$ ($x = N, P, As, Sb$). *Sci. Rep.* **6**, 1 (2016).
20. Kawaguchi, N., Urata, T., Hatano, T., Iida, K. & Ikuta, H. Nonmonotonic and anisotropic magnetoresistance effect in antiferromagnet CaMn $_2$ Bi $_2$. *Phys. Rev. B* **97**, 140403 (2018).
21. Gui, X. *et al.* Pressure-induced large volume collapse, plane-to-chain, insulator to metal transition in CaMn $_2$ Bi $_2$. *Inorg. Chem.* **58**, 8933 (2019).
22. Gibson, Q. *et al.* Magnetic and electronic properties of CaMn $_2$ Bi $_2$: A possible hybridization gap semiconductor. *Phys. Rev. B* **91**, 085128 (2015).
23. Zada, Z., Laref, A., Murtaza, G., Zeb, A. & Yar, A. First-principles calculations of electronic and magnetic properties of XMn $_2$ Y $_2$ ($X = Ca, Sr; Y = Sb, Bi$) compounds. *Int. J. Modern Phys. B* **33**, 1950199 (2019).
24. Piva, M. *et al.* Putative hybridization gap in CaMn $_2$ Bi $_2$ under applied pressure. *Phys. Rev. B* **100**, 045108 (2019).
25. Hundley, M., Canfield, P., Thompson, J., Fisk, Z. & Lawrence, J. Hybridization gap in Ce $_3$ Bi $_4$ Pt $_3$. *Phys. Rev. B* **42**, 6842 (1990).
26. Cooley, J., Aronson, M. & Canfield, P. High pressures and the kondo gap in Ce $_3$ Bi $_4$ Pt $_3$. *Phys. Rev. B* **55**, 7533 (1997).
27. Campbell, D. J. *et al.* High pressure kondo insulator-semimetal transition in Ce $_3$ Bi $_4$ Pt $_3$. [arXiv:1907.09017](https://arxiv.org/abs/1907.09017) (2019).
28. Sangeetha, N., Smetana, V., Mudring, A.-V. & Johnston, D. Antiferromagnetism in semiconducting SrMn $_2$ Sb $_2$ and BaMn $_2$ Sb $_2$ single crystals. *Phys. Rev. B* **97**, 014402 (2018).
29. Furness, J. W. *et al.* An accurate first-principles treatment of doping-dependent electronic structure of high-temperature cuprate superconductors. *Nat. Commun. Phys.* **1**, 11 (2018).
30. Lane, C. *et al.* Antiferromagnetic ground state of La $_2$ CuO $_4$: A parameter-free ab initio description. *Phys. Rev. B* **98**, 125140 (2018).
31. Zhang, Y. *et al.* Competing stripe and magnetic phases in the cuprates from first principles. *Proc. Natl. Acad. Sci.* **117**, 68 (2020).
32. Nokelainen, J. *et al.* Ab initio description of the Bi $_2$ Sr $_2$ CaCu $_2$ O $_{8+\delta}$ electronic structure. *Phys. Rev. B* **101**, 214523 (2020).
33. Pokharel, K. *et al.* Ab initio description of the electronic structure of high-temperature cuprate superconductors: A comparative density functional study. [arXiv preprint arXiv:2004.08047](https://arxiv.org/abs/2004.08047) (2020).
34. Lane, C. *et al.* First-principles calculation of spin and orbital contributions to magnetically ordered moments in Sr $_2$ IrO $_4$. *Phys. Rev. B* **101**, 155110 (2020).
35. Varignon, J., Bibes, M. & Zunger, A. Origin of band gaps in 3d perovskite oxides. *Nat. Commun.* **10**, 1658 (2019).
36. Dudarev, S., Botton, G., Savrasov, S., Humphreys, C. & Sutton, A. Electron-energy-loss spectra and the structural stability of nickel oxide: An LSDA+U study. *Phys. Rev. B* **57**, 1505 (1998).
37. Wang, Y.-C., Chen, Z.-H. & Jiang, H. The local projection in the density functional theory plus U approach: A critical assessment. *J. Chem. Phys.* **144**, 144106 (2016).
38. Han, X. *et al.* Limitation and extrapolation correction of the GGA+U formalism: A case study of Nb-doped anatase TiO $_2$. *J. Mater. Chem. C* **1**, 3736 (2013).
39. Lee, K.-W. & Pickett, W. Infinite-layer LaNiO $_2$: Ni $^{1+}$ is not Cu $^{2+}$. *Phys. Rev. B* **70**, 165109 (2004).
40. Madsen, G. K. H. & Novák, P. Charge order in magnetite: An LDA+U study. *EPL Europhys. Lett.* **69**, 777 (2005).
41. Blaha, P. *et al.* wien2k An augmented plane wave+local orbitals program for calculating crystal properties (2001).
42. Lipp, M. J. *et al.* Anomalous elastic properties across the γ to α volume collapse in cerium. *Nat. Commun.* **8**, 1 (2017).
43. Kugel, K. I. & Khomskii, D. The jahn-teller effect and magnetism: Transition metal compounds Soviet. *Phys. Uspekhi* **25**, 231 (1982).
44. Boswell, F. & Prodan, A. Peierls distortions in NbS $_3$ and NbSe $_3$. *Phys. B+C* **99**, 361 (1980).
45. Wilson, J. A. & Yoffe, A. The transition metal dichalcogenides discussion and interpretation of the observed optical, electrical and structural properties. *Adv. Phys.* **18**, 193 (1969).
46. Kertesz, M. & Hoffmann, R. Octahedral vs. trigonal-prismatic coordination and clustering in transition-metal dichalcogenides. *J. Am. Chem. Soc.* **106**, 3453 (1984).
47. Zhang, T. *et al.* Catalogue of topological electronic materials. *Nature* **566**, 475 (2019).
48. Vergniory, M. *et al.* A complete catalogue of high-quality topological materials. *Nature* **566**, 480 (2019).
49. Bradlyn, B. *et al.* Topological quantum chemistry. *Nature* **547**, 298 (2017).
50. Vergniory, M. *et al.* Graph theory data for topological quantum chemistry. *Phys. Rev. E* **96**, 023310 (2017).
51. Elcoro, L. *et al.* Double crystallographic groups and their representations on the Bilbao crystallographic server. *J. Appl. Crystallogr.* **50**, 1457 (2017).
52. Aroyo, M. I. *et al.* Crystallography online: Bilbao crystallographic server. *Chem. Commun.* **43**, 183 (2011).
53. Aroyo, M. I. *et al.* Bilbao crystallographic server: I: Databases and crystallographic computing programs. *Cryst. Mater.* **221**, 15 (2006).
54. Aroyo, M. I., Kirov, A., Capillas, C., Perez-Mato, J. & Wondratschek, H. Bilbao. crystallographic server: ii—Representations of crystallographic point groups and space groups. *Acta Crystallogr. A* **62**, 115 (2006).
55. Kresse, G. & Joubert, D. From ultrasoft pseudopotentials to the projector augmented-wave method. *Phys. Rev. B* **59**, 1758 (1999).
56. Kresse, G. & Furthmüller, J. Efficient iterative schemes for ab initio total-energy calculations using a plane-wave basis set. *Phys. Rev. B* **54**, 11169 (1996).
57. Kresse, G. & Hafner, J. Ab initio molecular dynamics for open-shell transition metals. *Phys. Rev. B* **48**, 13115 (1993).
58. Perdew, J. P., Burke, K. & Ernzerhof, M. Generalized gradient approximation made simple. *Phys. Rev. Lett.* **77**, 3865 (1996).
59. Cordier, G., Schäfer, H. & Naturforsch, Z. Neue intermetallische Verbindungen im anti-Ce $_2$ O $_2$ S-Strukturtyp/new intermetallic compounds in the anti-Ce $_2$ O $_2$ S-structure type. *B Chem. Sci.* **31**, 1459 (1976).

Acknowledgements

This work was supported by the U.S. DOE NNSA Under Contract No. 89233218CNA000001 and by the Center for Integrated Nanotechnologies, a DOE BES user facility, in partnership with the LANL Institutional Computing Program for computational resources. Additional support was provided by DOE BES Core Programs (LANL Codes: E3B5 and E1FR). M. M. Piva acknowledges the São Paulo Research Foundation (FAPESP) Grants 2015/15665-3, 2017/25269-3, 2017/10581-1.

Author contributions

C.L. and J.Z. performed computations, C.L., M.P., P.R., and J.Z. analyzed the results. J.Z. led the investigations and provided computational infrastructure. All authors contributed to the writing of the manuscript.

Competing interests

The authors declare no competing interests.

Additional information

Supplementary Information The online version contains supplementary material available at <https://doi.org/10.1038/s41598-023-35812-2>.

Correspondence and requests for materials should be addressed to C.L. or J.-X.Z.

Reprints and permissions information is available at www.nature.com/reprints.

Publisher's note Springer Nature remains neutral with regard to jurisdictional claims in published maps and institutional affiliations.



Open Access This article is licensed under a Creative Commons Attribution 4.0 International License, which permits use, sharing, adaptation, distribution and reproduction in any medium or format, as long as you give appropriate credit to the original author(s) and the source, provide a link to the Creative Commons licence, and indicate if changes were made. The images or other third party material in this article are included in the article's Creative Commons licence, unless indicated otherwise in a credit line to the material. If material is not included in the article's Creative Commons licence and your intended use is not permitted by statutory regulation or exceeds the permitted use, you will need to obtain permission directly from the copyright holder. To view a copy of this licence, visit <http://creativecommons.org/licenses/by/4.0/>.

© The Author(s) 2023